


RESEARCH ARTICLE

# CFD modelling of micro turbomachinery blade: integrating surface roughness with novel reverse-engineering strategies

Q. Yu  and R. Howell

School of Mechanical, Aerospace and Civil Engineering, The University of Sheffield, Sheffield, UK

**Corresponding author:** Q. Yu; Email: [qjmingyu.alex@gmail.com](mailto:qjmingyu.alex@gmail.com)

**Received:** 30 May 2024; **Revised:** 7 November 2024; **Accepted:** 7 November 2024

**Keywords:** micro gas turbine (MGT); computational fluid dynamics (CFD); surface roughness; reverse-engineering (RE); turbomachinery aerodynamics; gas turbine blade modelling

## Abstract

This paper presents the results of reverse-engineering (RE) strategies, surface roughness and computational fluid dynamics (CFD) modelling for a Wren100 micro gas turbine (MGT). Utilising silicone moulds and resin tooling, precise blade geometry capture was achieved for 3D reconstruction allowing for discrete and parametric geometric models to be created. Using these geometries, CFD simulations employing both Reynolds-averaged Navier–Stokes (RANS) and large eddy simulation (LES) models, alongside experimental wind tunnel cascade tests, were used to evaluate these reverse engineering strategies. The results show that while the parametric model captures overall MGT performance with fewer parameters, the discrete model provides enhanced accuracy, highlighting its suitability for detailed aerodynamic analyses. Contrary to initial expectations, surface roughness exhibited a noticeable impact on performance despite the lower Reynolds numbers (40,000), as demonstrated by the CFD model and wind tunnel experiments. The results indicate that surface roughness can reduce laminar separation bubbles on the blade leading edge, delay the onset of transition, and mitigate secondary flow losses. Overall, this study contributes to knowledge advancement in turbine blade reverse engineering and aerodynamics by detailing the impact of surface roughness on performance.

## Nomenclature

<i>MGT</i>	micro gas turbine
<i>CFD</i>	computational fluid dynamics
<i>RPM</i>	revolutions per minute
<i>RANS</i>	Reynolds-averaged Navier–Stokes
<i>LES</i>	large eddy simulation
$Re_k$	roughness Reynolds number
$k_s$	sand grain roughness
<i>RE</i>	reverse-engineering
<i>LE</i>	leading edge
<i>TE</i>	trailing edge
$R_z$	mean peak-to-valley height
$R_a$	average arithmetic roughness height
$y^+$	dimensionless wall distance
<i>P</i>	static pressure
$P_0$	total pressure
<i>U</i>	blade speed
$C_x$	flow axial velocity

$Pr$	pressure ratio
$Y_p$	stagnation pressure loss coefficient
$Re$	Reynolds number
$\dot{m}$	mass flow rate
$F$	thrust
$d$	diameter

### Greek symbol

$\alpha$	blade exit angle
$\beta$	blade wedge angle
$\gamma$	dimensionless wall distance
$\xi$	blade stagger
$\phi$	flow coefficient
$\psi$	stage loading coefficient
$\eta$	isentropic efficiency
$\theta$	blade wedge angle
$\alpha_2$	blade exit angle
$\rho$	density

## 1.0 Introduction

The definition of micro gas turbines (MGTs) is small turbomachines with a power output in the range between approximately 15–300KW [1]. Numerous MGTs have been developed over the years [2–5]. The lowest power engines (including the Wren series) in this range tend to be very small with turbine blade heights of around 10mm as well as have low-pressure ratios (2–3), relatively low turbine entry temperatures (around 1,000K), which together with low Reynolds numbers and high surface roughness to chord ratio in the turbine results in low cycle efficiencies [6, 7]. The applications of micro-scale turbomachinery are varied because they provide lightweight and compact alternatives in the field of electrical power generation and propulsion (both as turbojets and turboprops) in both civilian and military areas [8, 9]. Due to global climate change, developing higher efficiency micro gas turbine systems is necessary to reduce pollutant emissions and reduce fuel burn. ACARE (Advisory Council for Aviation Research and Innovation in Europe) requires that new technologies and procedures should be developed to allow a 75% reduction in CO<sub>2</sub> and a 90% reduction in NO<sub>x</sub> per passenger kilometre for new aircraft engines in 2050 compared to 2000 [10]. While this might not apply to MGTs directly, there is still a driver to reduce pollutants and increase the specific thrust of such units.

Conventional design starts with the performance requirement of the product and moves through a design process to the end product. In the case presented in this paper, an existing design was available, but there was no technical documentation. As a result, a reverse engineering (RE) process was required. This starts with the existing product and, through various techniques, ends up with a reconstruction of the geometry of the product [11]. Many techniques exist to obtain the geometry of the product, including contact and noncontact approaches, but they all have the same aim, i.e. to capture the most accurate representation of the geometry. However, selecting the most appropriate RE method to balance the most appropriate geometry accuracy versus the time taken (and so cost) involved is important.

To investigate the influence of surface roughness on the turbine performance, a numerical study was conducted by Gamil et al. on the Samad Power TwinGen micro gas turbine, which bears resemblance to the Wren100 with a slightly higher pressure ratio of 3 and RPM of 170,000 and Reynolds number between 50,000 and 250,000. They demonstrated that an increase in surface roughness from 3 to 6, 20 and 100 microns leads to a reduction in stage total efficiency by 0.8%, 4% and 12%, respectively, accompanied by a comparable decrease in output power by 0.7%, 3.6% and 11%, respectively. It was also discovered that the surface roughness could potentially impact the temperature of the turbine,

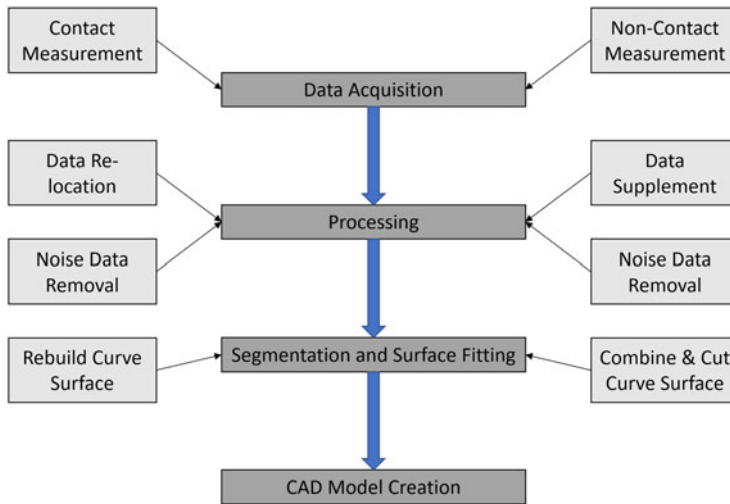


**Figure 1.** Contact & non-contact RE flow chart [15].

whereby heightened roughness may lead to an elevation in temperature at both the rotor hub and tip regions [12]. Bai et al. performed experimental investigations on blade cascades and reported that the velocity distribution within the boundary layer of the rough blade was comparatively more flattened than that of the smooth blade. Furthermore, it was observed that the aerodynamic loss for the rough blade remained lower for low Reynolds number flow, while it increased significantly for high Reynolds number flows [13].

This paper presents a detailed methodology for reverse-engineering MGT blades using a high-precision Alicona laser-scanning machine, complemented by both experimental validation and CFD modelling. Given the challenges posed by the small size of turbine blades (chord less than 10mm) and their high surface reflectivity, traditional laser scanning struggled to accurately capture the intricate details of the Wren100 turbine blades. To address this issue, the authors introduced a RE technique employing silicone moulds and resin tooling, enhancing scanning accuracy and the quality of subsequent reconstructions. This paper explored two distinct RE strategies: parametric and discrete modelling, each evaluated through targeted CFD simulations. The study then assesses the aerodynamic performance of the MGT, focusing on the discrete models (the most accurate representations of the turbine geometry) and examining the influence of surface roughness on the turbine performance. A series of advanced analyses provide a foundation for future in-depth analysis of the effects of surface roughness on MGT blade performance. This paper underscores the importance of different RE strategies in determining MGT aerodynamics, allowing more accurate performance (power output and efficiency) to be determined and providing improved turbine design.

### 1.1 Digitising methods for turbine blades RE

By testing various contact and non-contact equipment (see Fig. 1), Mahboubkhah et al. discovered that the reported information by the digitising equipment manufacturers is not always reliable, meaning experimental validations are always required for the RE models [14–16]. Thus, CFD simulations and experimental data were obtained in this study to investigate the performance of the RE models.

Following the acquisition of geometric data, the selection of an appropriate reverse engineering strategy is crucial, as it could either be based on ‘what the part actually is’ or ‘what the part could be’. The latter approach has been extensively investigated in the field of RE, with Mohaghegh et al. proposing a novel method to reverse engineer aerofoils from existing turbine blades based on design intent,

emphasising the importance of ‘what the part could be’. Incorporating essential design points is shown to be vital during the RE process as measurement equipment can introduce significant uncertainties [17]. She and Chang introduced a novel RE process for turbine blade disks, demonstrating the feasibility of modern computer-aided design techniques to reconstruct complex turbine geometries [18]. Li et al. proposed a novel parameterisation approach for the RE of turbine blades, in which essential features were extracted from the point cloud data to reconstruct blade geometry based on aerodynamic rules [19]. Most existing studies on the RE of turbine blades have focused on ‘what the part could be’, as smooth surfaces are typically required to achieve high aerodynamic efficiency [20]. Moreover, previous research has not given much attention to the RE of MGTs compared to conventional gas turbines.

## 2.0 Computational methods for turbomachinery blades

Turbomachinery blades operating under low Reynolds numbers typical of MGTs means there is a substantial amount of transitional flow, which calls for appropriate modelling approaches. The RANS approach offers a pragmatic balance between computational demand and predictive capability. For example, the study by Lakehal utilised near-wall modelling to enhance the fidelity of film cooling predictions on turbine blades, validating the RANS model against direct numerical simulation data, underscoring its utility [21]. Guo et al. showed that RANS models were adept at capturing fundamental aerothermal behaviours in turbine blade channels, providing reliable insights into the complex interactions within rotating channels [22]. Similarly, Sofi and Qayoum utilised RANS to analyse heat transfer and flow loss, demonstrating the significant influence of rib shapes within cooling ducts on the overall thermal efficiency of gas turbines [23].

Incorporating a transitional model in RANS results in more accurate predictions at low Reynolds number flows found in MGTs [24]. While RANS provides a computationally efficient overview of flow fields, LES offers higher-fidelity detail, capturing complex turbulence and flow separation, as evidenced in studies by Dong and Amano [25]. Furthermore, the integration of RANS and LES models allows for a comprehensive performance optimisation strategy, as demonstrated by He et al., where an automated optimisation platform for turbine blades leveraged RANS techniques [26]. The optimisation led to improved efficiency and addressed severe flow separation issues, underscoring the versatility of RANS in multi-objective, multi-condition scenarios. To address intricate internal cooling challenges, Kim et al. showcased how RANS simulations could be validated against LES and experimental data, proving the potential of RANS models in predicting convective heat transfer [27]. The accuracy of RANS in studying complex cavity designs, as revealed by Xiao et al. and Ju et al., further justifies its application in this research [28, 29].

The combination of RANS and LES methodologies in this paper allows LES to complement the RANS approach, providing detailed insights where RANS’ predictive scope is limited. This dual-method approach is validated by empirical studies such as Schreiner et al. and Saleh et al., providing a computational framework for the intricate aerodynamic analysis required to study micro gas turbine blades [30, 31].

### 2.1 Wall model for surface roughness

Several modifications have been proposed to account for the influence of surface roughness in near-wall regions using RANS and LES simulations. This study employs the Colebrook formula to estimate the roughness function ( $\Delta B$ ), which is appropriate for hydraulically rough surfaces characterised by uniform sand-grain roughness. However, this might not be effective for more complex roughness patterns, such as those with non-uniform or anisotropic roughness. Jimenez suggests that these limitations could contribute to modelling inaccuracies when surfaces deviate significantly from the uniform roughness assumption [32].

For surfaces with more complex roughness types, alternative models may provide more accurate predictions but are not available in the computational code used here (ANSYS CFX 19.2, described

later). For example, the Nikuradse model, which characterises roughness through equivalent sand grain roughness, has been successfully used for surfaces with uniform roughness distributions. The roughness length scale (RLS) model, on the other hand, is better suited for anisotropic roughness elements as it incorporates directional effects, making it appropriate for cases where roughness elements are not uniformly distributed. Similarly, Flack et al. propose a parameterisation approach that considers both the height and spatial distribution of roughness elements, potentially improving the accuracy of turbulent flow predictions over complex surfaces [33].

In this research, to activate the roughness factor in ANSYS CFX, a downstream shift in the logarithmic velocity profile equation is used, as shown in Equation (1) [34]:

$$u^+ = \frac{1}{\kappa} \ln(y^+) + B - \Delta B \tag{1}$$

The downstream shift can be described as a dimensionless function of the roughness height, where  $B$  is an empirical factor of 5.2, according to previous experimental studies [34].

$$\Delta B = \frac{1}{\kappa} \ln(1 + 0.3Re_k) \tag{2}$$

$$Re_k = \frac{k_s u_\tau}{\nu} \tag{3}$$

In Equation (3), the  $k_s$  represents the function of sand grain roughness, which the three regions of the model would be determined by the roughness Reynolds number ( $Re_k$ ). There are three regimes of roughness, which are listed as follows [34].

- Hydraulically smooth ( $0 < Re_k < 5$ );
- Transitional rough ( $5 < Re_k < 70$ );
- Fully rough ( $70 < Re_k$ );

To represent the shape and spacing of the roughness elements, the roughness constant ( $C_s$ ) is often used. The Nikuradse model, for example, characterises roughness through equivalent sand grain roughness and has been effective for surfaces with a more uniform roughness distribution. Recent studies have continued to validate and extend the findings of Nikuradse, particularly in their application to turbulent flow over rough surfaces [32, 35]. In some applications, the CFD codes combine the  $\Delta B$  into a modified formulation of near-wall kinematic viscosity ( $E$ ). The Equation (1) can be re-arranged into Equations (4) and (5).

$$u^+ = \frac{1}{\kappa} \ln\left(\frac{E y^+}{e^{\Delta B}}\right) = \frac{1}{\kappa} \ln(E' y^+) \tag{4}$$

$$E' = e^{\Delta B} \tag{5}$$

According to the manual, the commercial CFD codes solve the wall roughness in the following five steps [34].

1. Proceed to the boundary cell face
2. Calculate  $y^+$  and  $Re_k$
3. Calculate  $\Delta B$  or  $E'$
4. Calculate  $\nu_w$
5. Resolve momentum equations of  $u^+$

Despite the wide application of roughness modification functions, several previous studies have highlighted the challenges of using current commercial CFX codes to simulate surface roughness effects accurately. Alldieck et al. investigated the interaction of transition and turbulence models with rough

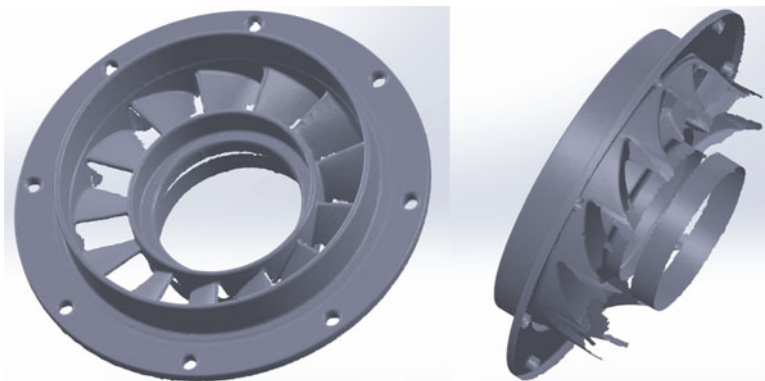


**Figure 2.** *Wren100 stator direct laser scan (missing details near trailing edge).*

wall boundary conditions using the TRACE solver. They found that, although the model itself was not designed to be sensitive to surface roughness, the rough wall still influenced the transition process. However, none of the model combinations tested could precisely replicate the experimental results [36]. Similarly, Blocken et al. researched various commercial CFD codes, including ANSYS Fluent and CFX, and noted that CFD results can vary significantly depending on the type of roughness modification applied to the wall functions. They concluded that further improvements are needed in modelling rough wall effects, particularly in predicting the onset of transition [37].

### 3.0 Non-contact measurement process of the wren100 turbine blade – general workflow

Wren Power Systems (now Turbine Power Solutions) Ltd. originally designed the Wren100 turbine to serve as a component of a micro turbojet engine. This turbine comprises an axial turbine with 13 stator vanes and 21 rotor blades, with a span of roughly 10mm. Given the micro size of the Wren100 turbine parts and the intricacy of their twisted profiles at varying blade heights, direct laser scanning of their 3D geometries has proven exceedingly challenging.

Figure 2 reveals that the 3D geometry acquired lacks numerous details near the trailing edge (TE) due to high surface reflectance and light blockage. As a result, the stator and rotor blades were reconstructed using silicone rubber moulds and epoxy (EP) resin to enhance the quality of the laser-scanned models. Initially, liquid silicone rubber (Limino two-part platinum-cured elastomer) was employed to produce moulds of the Wren100 stator and rotor blades. The liquid silicone rubber was poured separately into two containers at a mixing ratio of 1:1 [38]. Subsequently, once the rubber had solidified, the stator and rotor blades were removed from their containers, leaving behind cavities that could be utilised to create models. Each vane and blade was labelled after they had been removed from the solidified silicone rubber for future geometrical acquisition. The next step involved injecting liquid EP resin into the silicone rubber moulds to reconstruct the Wren100 stator and rotor blades. The injection process of the liquid EP resin was similar to that of the liquid silicone rubber, with a mixing ratio of 1:1 for the resin and hardener [39]. To increase the surface reflectance of the blade models, white paint was blended with the liquid EP resin. Once the EP resin had solidified, the Wren100 stator and rotor blade models were removed from the silicone rubber moulds (Fig. 3).

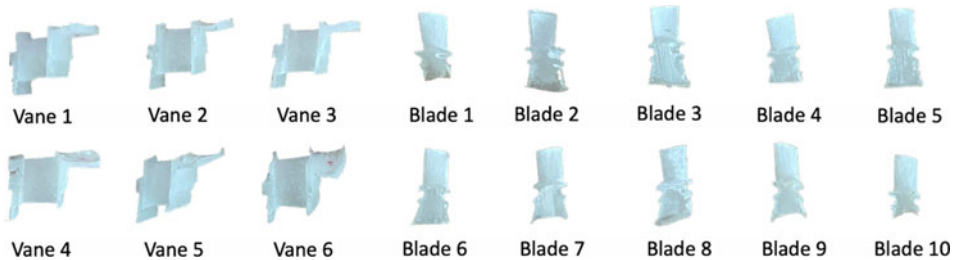
To assess the quality of the EP resin-rebuilt models, surface roughness measurements were conducted on both the original and RE blades using the InfiniteFocusSL system, a high-precision roughness tester developed by Bruker Alicona [40, 41]. The results in Table 1 demonstrate minimal differences in average surface roughness height between the original metal blades and the EP resin models. These findings confirm the suitability of the EP resin models for reverse engineering applications.

**Table 1.** Wren100 stator (13 vanes) and rotor surface roughness (21 blades)

Samples	$R_a$ ( $\mu\text{m}$ )	$R_z$ ( $\mu\text{m}$ )	$R_{sk}$ ( $\mu\text{m}$ )	$R_{ku}$ ( $\mu\text{m}$ )	$R_a/\text{Chord}$	$R_z/\text{Chord}$
Stator (original)	2.472	14.722	-0.251	3.397	0.000163	0.00097
Stator (EP resin)	2.005	11.932	-0.045	3.755	0.000132	0.000786
Rotor (original)	2.606	15.195	0.713	6.474	0.000361	0.00211
Rotor (EP resin)	2.433	15.174	0.183	4.881	0.000337	0.0021

Note:  $R_a$ ,  $R_z$ ,  $R_{sk}$  and  $R_{ku}$  indicate average roughness measurements.

<sup>a</sup>Detail about surface roughness specifications.

**Figure 3.** EP resin models of Wren100 stator vanes and rotor blades (samples).

As presented in Table 1, the maximum average roughness difference between the original turbine parts and the EP resin models is approximately  $2.79\mu\text{m}$ , which is a relatively small deviation given the scale of the MGT. However, it is worth noting that the  $R_z$  value, representing peak-to-valley roughness, shows more significant differences for the stator surfaces. The original stator has an  $R_z$  of  $14.722\mu\text{m}$ , while the EP resin stator model exhibits a lower  $R_z$  of  $11.932\mu\text{m}$ , corresponding to a 19% reduction. This difference indicates that the EP resin moulding process produces smoother surface features than the original metal parts.

Despite these differences, the EP resin models were used to capture the basic geometric shapes of the stator and rotor blades, with the primary goal being to facilitate accurate reverse engineering using laser scanning. The small roughness deviations between the EP resin models and the original parts demonstrate that the EP resin models are an acceptable option for this reverse-engineering process. It is important to highlight that the surface roughness characteristics, such as  $R_z$ ,  $R_{sk}$  and  $R_{ku}$ , could not be introduced into the CFX simulations due to solver limitations. Nonetheless, the values of  $R_{sk}$  (skewness) and  $R_{ku}$  (kurtosis) provided for the original turbine parts are included to show how these parameters might potentially influence aerodynamic performance, even though they were not used in the current study. While these factors were not directly applicable here, they represent important considerations for roughness modelling in future studies.

### 3.1 Data acquisition system (laser-scanning)

An EinScan Pro 2X laser scanner was employed to obtain the turbine geometry from the resin models. During the scanning process, the software generates millions of points, which are subsequently merged to re-create the geometry. Obtaining the surface details of all sides of the object may require multiple scans, sometimes numbering in the hundreds. The software then aligns these scanned points to generate the whole model, a process known as registration or alignment [42, 43]. Following the alignment of the multiple scanned data, the 3D description of the turbine parts can be exported to a standard tessellation language file and imported into ANSYS SpaceClaim for further RE processing. In the RE of the Wren100 turbine, point clouds of the 13 stator vanes and 21 rotor blades were acquired, each consisting of millions of coordinates. Consequently, to generate 3D solid geometries, the profiles at different radial heights were captured from each stator vane and rotor blade.



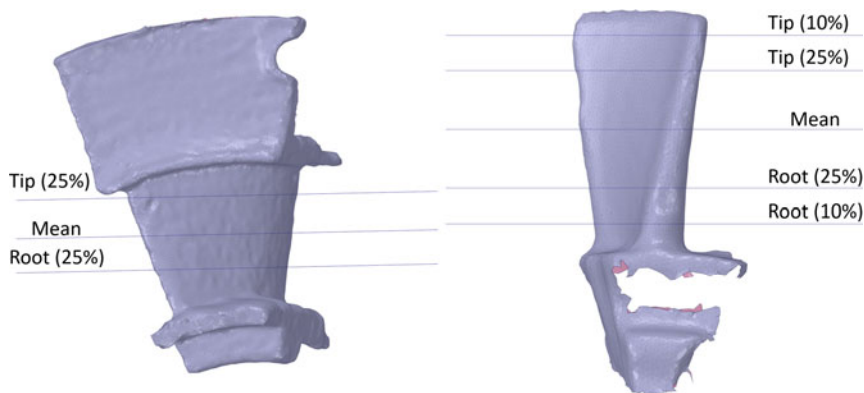


**Figure 4.** *Stator and rotor profiles acquisition (root, mean and tip).*

Figure 4 illustrates the acquisition of profiles at various radial heights for the stator vanes and rotor blades of the Wren100 turbine. Three sections of profiles were obtained for the stator vanes, situated at 25% span from the root (root (25%)), mean, and 25% span from the tip (tip (25%)). The root and tip sections were not directly captured due to blockage by the stator shroud, which can result in incomplete scanned data near these sections. In contrast, the rotor disk has no shroud, allowing for closer proximity laser-scanned quality to the root and tip sections (10% span). The scanned data was plotted in a Cartesian system to obtain average profile coordinates at different radial blade heights. In order to ensure smooth profile changes at different radial heights, linear interpolation was utilised to acquire 2D profiles at the root and tip sections, providing a better understanding of the original design intent. Finally, an appropriate reverse engineering strategy was selected to obtain the three-dimensional geometries of the stator and rotor, as detailed in the following subsections.

#### 4.0 RE strategies

The design of a turbine blade normally requires the engineer to handle lots of parameters, including chord, stagger, pitch, etc. Thus, the important question in the field of RE is whether to consider all of those parameters or just use some essential characteristics to re-create the model. The RE strategies can often be divided into ‘what the part really is’ (discrete) and ‘what the part could be’ (parametric). In this research, the 3D blade geometries were re-constructed and compared based on discrete and parametric strategies. For the discrete strategy, all the original design parameters were considered for the RE model by applying spline to the average scanned profile coordinates. The parametric strategy used ANSYS BladeGen, which can be used to rebuild the 3D geometry by choosing seven parameters of the blade (leading edge (LE) and trailing edge (TE) diameters, LE Beta angle, exit angle, blade stagger, LE and TE wedge angle). The detailed comparison of the RE models based on two strategies are described in Subsections 4.1 and 4.2.

##### 4.1 Discrete – ‘what the part really is’

The first RE strategy is directly generating splines from the averaged data points to create different layers of profiles, in which the two-dimensional shape information was applied to re-create the three-dimensional reconstruction of one stator vane and one rotor blade in detail. With the profiles at different blade heights, the stator vane and rotor blades were then automatically generated by CAD software.



**Table 2.** Wren100 stator and rotor blade characteristics

Section	$d_{LE}$ (mm)	$d_{TE}$ (mm)	$\alpha_2$ (°)	$\xi$ (°)	$\theta_{LE}$ (°)	$\beta_{LE}$ (°)	$\theta_{TE}$ (°)
<i>Stator</i> <sub>Root</sub>	1.4	1.0	59.5	34.5	2.0	15.0	0.0
<i>Stator</i> <sub>Mean</sub>	1.3	1.0	65.0	43.5	9.0	6.0	1.5
<i>Stator</i> <sub>Tip</sub>	1.3	1.2	66.0	49.0	10.5	0.0	2.0
<i>otor</i> <sub>Root</sub>	5.6	1.2	45.0	15.0	27.0	27.0	4.5
<i>Rotor</i> <sub>Mean</sub>	1.1	0.9	55.0	37.2	21.0	9.0	3.8
<i>Rotor</i> <sub>Tip</sub>	0.9	0.6	62.0	50.4	15.0	3.0	3.3

Note: Specifications refer to various measurements of the rotor and stator blades.

<sup>a</sup>Details for  $d_{LE}$  and  $d_{TE}$  refer to leading and trailing edge diameters, respectively.

<sup>b</sup>Angles  $\alpha_2$ ,  $\xi$ ,  $\theta_{LE}$ ,  $\beta_{LE}$  and  $\theta_{TE}$  refer to specific geometric properties of the blades.

## 4.2 Parametric – ‘what the part could be’

The second approach to RE involves the reconstruction of its three-dimensional geometries by using blade parameters, which are obtained through the identification of base circles for the LE and TE. The base circle location was determined by an iterative process whereby circles were initially drawn based on points 1, 4 and 7 of the pressure side (PS) and suction side (SS) groups. The circle was then shifted one point forward to fit accordingly to points 2, 5, and 8. This process was repeated until the circle covered most of the points on one side of the aerofoil. Finally, the smallest circles that are tangent to the PS and SS circles were identified as the base circles. It should be noted that the base circles may not cover all the points due to the rough surface of the laser-scanned model. However, since the goal is to recreate the original part as closely as possible, the blade characteristics obtained from the base circles are still acceptable for further reverse engineering. Table 2 presents the Wren100 stator and rotor blade characteristics, including the root, mean and tip sections of both components.

With the acquired blade characteristics, the three-dimensional geometries of the Wren100 stator and rotor were re-created by using ANSYS BladeGen.

## 5.0 CFD modelling of the wren100 stator-rotor with error calculations

CFD simulations were conducted to verify the accuracy of the reverse-engineered turbine using the two different RE strategies compared to the experimental results. The experimental results and an iterative process were used to provide the necessary initial input and results validations for the CFD simulations.

### 5.1 Initial boundary conditions based on experimental tests

As shown in Fig. 5, the Wren100 jet engine was mounted on a test bed connected to a force sensor that can be used to measure the thrust generated. Eight static pressure transducers and eight thermocouples were connected to different positions of the jet engine to provide real-time inlet pressure and temperature sensing.

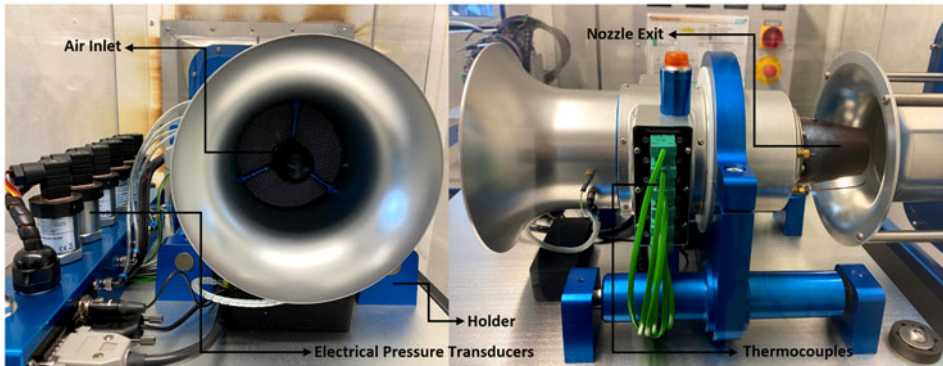
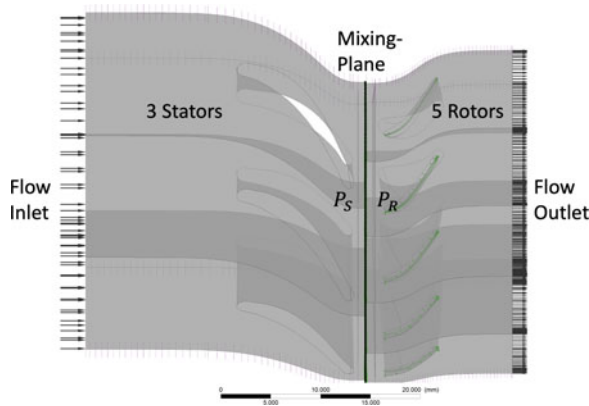
The engine was tested at five rotational speeds that vary from 100k to 140krpm. LabView was used to store data acquired by the pressure and temperature sensors at a rate of 1Hz. At the start of a test, the jet engine would pre-heat itself until the RPM reached 50krpm. Then, the throttle control on the control panel was used to adjust the RPM required for the testing. As shown in Table 3, with the acquired experimental data, time-averaged values of the test results were logged to provide a database for further CFD inputs and results validation.

### 5.2 CFD mesh generation and verification

The fluid domain of the stator-rotor system is displayed in Fig. 6, which has three stators and five rotors with a mixing plane to ensure the pitch ratio is close to one. Many types of mesh (structured, unstructured or hybrid) have been used to simulate gas turbine blades [44]. In this study, structured cells were automatically generated by the ANSYS TurboGrid for the turbine passages, as shown in Fig. 7. For the computational domain of the rotor blades, the 5% tip clearance was also included.

**Table 3.** Wren100 engine test results

$T_{01}$ (K)	$P_2$ (bar)	$\dot{m}$ (kg/s)	$F$ (N)	RPM
1,310	0.699	0.146	53.4	140k
1,232	0.737	0.133	40.1	130k
1,081	0.901	0.115	27.5	120k
1,056	0.896	0.100	19.9	110k
1,027	0.897	0.088	13.1	100k

**Figure 5.** Wren100 experimental instrumentations.**Figure 6.** Computational domain with periodic boundary conditions.

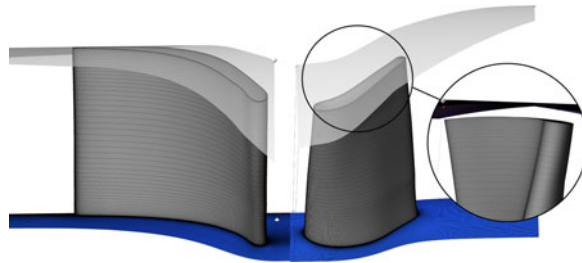
As shown in Fig. 7, constant tip clearance was used based on the reverse-engineered blade data.

### 5.3 Wren100 engine test error estimation based on an iterative CFD method

Many studies have shown the existence of total temperature non-uniformity in the regions between the combustion chamber and the stator inlet [45]. Due to the inlet total temperature being measured at a single point before the stator, it is uncertain whether the value can represent the true operating condition. The static pressures measured in the nozzle regions are likely to have an error due to the static tube not being flush with the nozzle surface. Therefore, the only reliable data from the engine are the mass flow rate and thrust. Iterative CFD simulations were conducted with the two different RE geometries and

**Table 4.** RANS  $\gamma - \theta$  transition model and LES WALE model parameters

Parameter	RANS Gamma-Theta SST	LES WALE
Transition model	Gamma-Theta 4-equation	N/A
Turbulence model	SST	WALE
Near-wall refinement	Yes	Yes
Turbulent kinetic energy	Modeled	Partially resolved
Wall treatment	Fully modeled	Wall-modeled (WMLES)
Time stepping scheme	N/A	Second-order backward Euler
Time step size	N/A	$3.97 \times 10^{-7}$ seconds
Number of time step	N/A	60

**Figure 7.** Wren100 mesh generated by ANSYS TurboGrid ( $y^+ < 1$ ).

these boundary conditions to determine the correct overall boundary conditions for the turbine (see Section 8).

This study initially chose a four-equation transitional turbulence model based on anticipating substantial transitional flow. The rationale behind selecting a transitional turbulence model is supported by empirical evidence from the literature, notably the findings from Sanders et al. Their work underscores the superior capability of transitional models in capturing the flow physics associated with low Reynolds number regimes, including the critical phenomena of boundary layer separation and transition. Specifically, the study by Sander et al. provides a compelling argument for the application of such models by showcasing improved accuracy in predicting aerodynamic performance, particularly in scenarios where conventional models may fall short due to their inability to account for the complex transitional flow characteristic of MGT environments [46].

In addition to the RANS simulations, the LES wall-adapting local eddy-viscosity (WALE) model was incorporated into this study by first performing a steady-state RANS simulation and then using the RANS solution to initialise the LES simulation (Table 4). This approach enables the LES simulation to start with an already well-developed flow field, thereby improving convergence and accuracy in capturing the detailed turbulence structures. It is important to clarify that this procedure does not represent a hybrid method like detached eddy simulation (DES) or a zonal approach. Instead, the LES was initialised with the RANS results, allowing for a sequential simulation strategy where RANS provides the broad flow features and LES is employed for detailed turbulence analysis. The LES WALE model was selected for its proven ability to accurately simulate wall-bounded flows, which are common in turbomachinery applications. Studies such as Kim et al. have demonstrated the capability of the WALE model in predicting the transitional flow regimes often found in MGT blade passages [47]. This approach is in line with best practices in turbomachinery analysis, as described by Dufour and Rosa [48].

Due to limitations in computational resources, the same mesh used for the RANS simulations was employed for the LES simulations. A preliminary verification process, as shown in Fig. 8, indicated that a minimum of 5,300,000 elements for the stator and 6,000,000 for the rotor were required to achieve

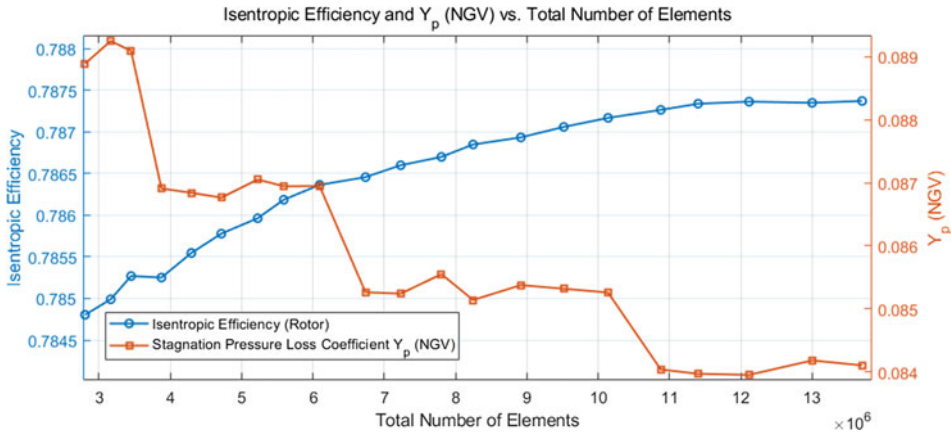


Figure 8. Wren100 CFD model verification (RANS  $\gamma - \theta$  transition model).

reliable results. A mesh independence study confirmed that this mesh density was sufficient for accurate flow resolution in the RANS simulations. Given these results and the computational constraints, the same mesh was applied in the LES simulations despite the finer mesh typically required by LES, especially near-wall regions for resolving small-scale turbulence. Despite this compromise, the LES predictions closely aligned with those of the RANS simulations. The RANS and LES results were validated against experimental data obtained from wind tunnel cascade tests, as discussed in the later section. These tests demonstrated that the simulations effectively reproduced the aerodynamic behaviour of the turbine components, further supporting the adequacy of the chosen mesh for both RANS and LES simulations.

Based on the verified CFD model, iterative simulations were carried out to determine the true boundary conditions of the Wren100 turbine. Due to the lack of correct information at the nozzle, the outlet total pressure used for iterations was acquired from the experimental research conducted by Golchin et al. on the same engine [49]. With the essential boundary conditions, the iteration process is described as follows. Firstly, an initial CFD simulation was conducted based on the experimental data to generate the nozzle exit velocities. The exit static pressure ( $P_2$ ) in the simulations was computed as a mass-averaged value using ANSYS CFX post, ensuring an accurate representation of the flow characteristics at the nozzle outlet. Then, as the nozzle is known to be un-choked, according to the known exit total pressure, the static pressure can be estimated by Equation (6).

$$P_2 = P_{02} - \frac{1}{2} \rho C_2^2 \tag{6}$$

The predicted  $P_2$  can then be used as the updated information for the next CFD iteration. With the necessary geometric data, the updated inlet total temperature can also be estimated based on the stage loading coefficient as shown in Equation (7), in which the exit angles ( $\alpha$ ) were acquired from the RE models as demonstrated in Table 2 [50].

$$\psi = \frac{C_p \Delta T_0}{\frac{1}{2} U^2} = \frac{2C_x}{U} (\tan \alpha_2 + \tan \alpha_3) \tag{7}$$

Finally, the new boundary conditions can be put into the CFD solver for the updated iteration of  $P_2$  until the thrust and mass flow rate values converge to a constant value. The final base performance iterated from two different reverse-engineering strategies is demonstrated in the following subsection.

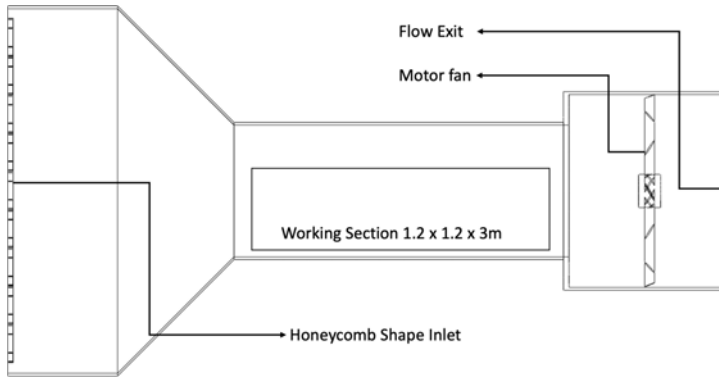


*Figure 9. Large wind tunnel schematic diagram.*

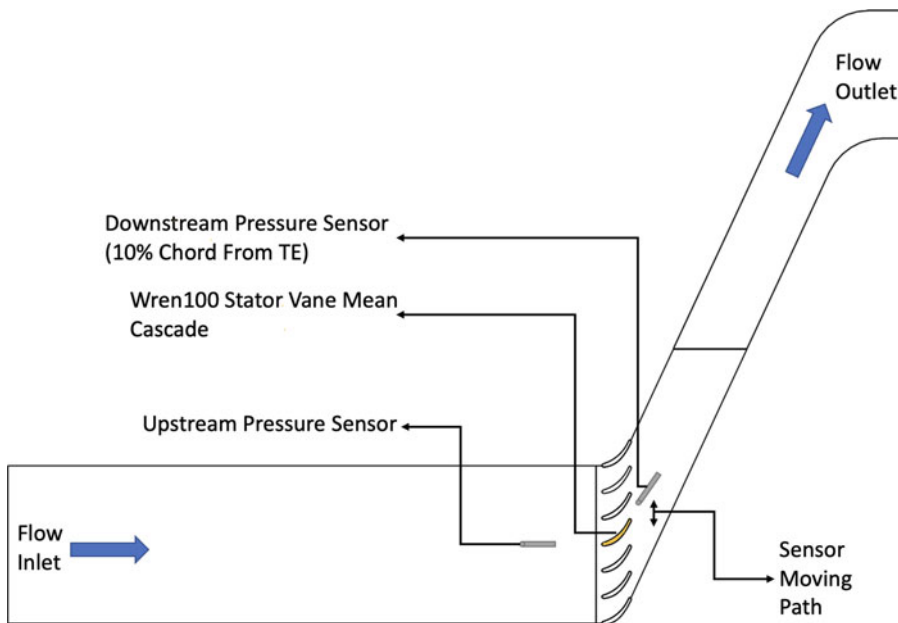


*Figure 10. Wren100 NGV mean cascade (lifted) schematic diagram.*

## 6.0 Wind tunnel cascade validations for the aerofoil models

Wind tunnel cascade tests were used to validate the aerofoil models based on RANS and LES techniques. Two different configurations of the cascade were tested, which are the scaled Wren100 stator vane mean section models with and without roughness elements. The experimental tests were performed in a wind tunnel located in the laboratory for experimental tests at the University of Sheffield. The schematic diagram of the large wind tunnel displayed in Fig. 9 is of a conventional design with a honeycomb flow straightener, convergent inlet, working section and fan.

The wind tunnel has a working section of  $1.2 \times 1.2 \times 3\text{m}$ , where the cascades and the data acquisition instrumentations were mounted. The contraction ratio is 6:1, and the rotational speed of the motor fan achieves the control of flow speed. The inlet to the cascade (Fig. 10) was placed in the middle of the wind tunnel so as to minimise the potential for the floor boundary layer to distort the flow conditions within the cascade rig [51].

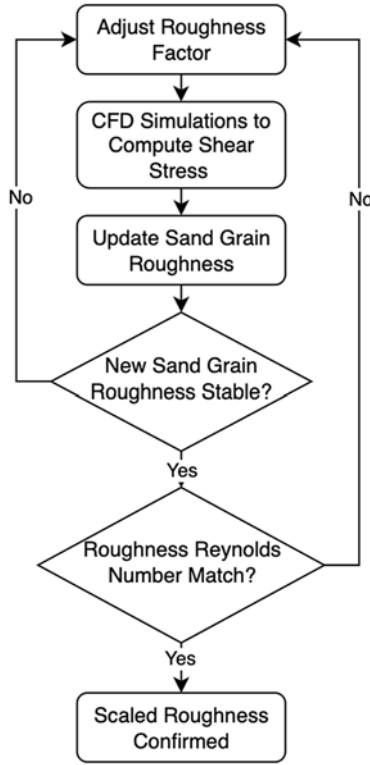


**Figure 11.** Flow diagram of iterative CFD simulations to acquire surface roughness of the scaled wind tunnel cascade model.

### 6.1 Roughness scale study

The RE model used for the study of surface roughness was the discrete model. When scaling the blade profile, one critical parameter is the roughness Reynolds number, which was scaled to match the engine. In this approach, the roughness factor was defined using a sand grain roughness height input in the CFX solver, without directly altering the surface geometry but using a wall-function approach to account for the roughness effects, as appropriate for high wall- $y^+$  cases.

$$k_{s,WT} = \frac{u_{\tau,o}}{u_{\tau,WT}} \cdot k_{s,o} = \sqrt{\frac{\tau_{w,o}}{\tau_{w,WT}}} \cdot k_{s,o} \quad (8)$$

In order to match the roughness Reynolds number, as depicted in Equation (8), obtaining the shear stress data on the scaled cascade blades is needed. However, this data can only be acquired through CFD simulations or experimental tests, which require prior knowledge of the surface roughness for the scaled model. An iterative study was conducted using CFD simulations, as illustrated in the flow diagram (Fig. 5).

Initially, a preliminary guess of the surface roughness for the scaled model was made by directly using the scaling factor (around 4.3), and this value was utilised to determine the shear stress data and a new surface roughness estimate. Subsequently, this updated surface roughness was employed to generate a refined rough model of the cascade blade for further simulations. This iterative process (Fig. 11) continued until the surface roughness data stabilised, indicating convergence and yielding the final surface roughness for the scaled model was acquired.

**Table 5.** Original stator roughness vs. target roughness for scaled wind tunnel cascade

Samples	Ave. $R_a$ ( $\mu\text{m}$ )	Ave. $k_s$ ( $\mu\text{m}$ )
Original profile	2.472	14.492
Scaled cascade	8.447	49.518

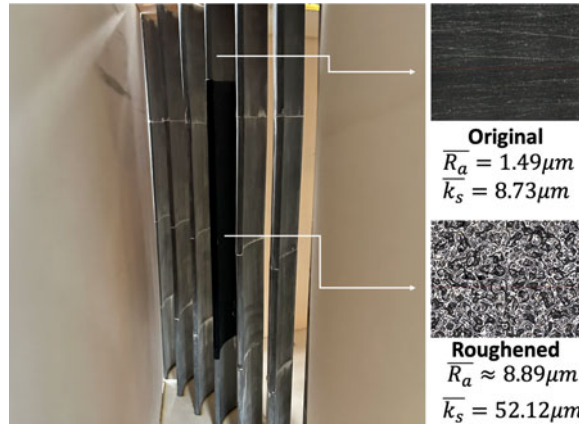


**Figure 12.** Sand-roughened wind tunnel cascade middle blade.

According to the calculated data listed in Table 5, the roughness Reynolds number was calculated as shown in Equation (9).

$$5 < Re_k = \frac{u_\tau k_s}{\nu} = 6.234 < 70 \quad (9)$$

From the calculated  $Re_k$ , it was discovered the regime of roughness for the stator blade is transitional rough, where the surface roughness elements start to have a noticeable impact on the flow field. To match the  $Re_k$  for the wind tunnel cascade with the original MGT stator vane, the arithmetic roughness of the 3D printed blade surface was increased and measured.

As shown in Fig. 12, the surface roughness of the middle blade was increased to near the required values ( $k_s \approx 50\mu\text{m}$ ) by attaching a piece of rough paper on the blade surface.

## 7.0 Model validation

### 7.1 Smooth model (discrete)

Figure 13 shows the graphical representations of the comparison, where the CFD results are plotted against the cascade results under two different Reynolds numbers. The plots demonstrate a strong correlation between the two datasets, further validating the CFD model.

Figures 13 show the flow 10% chord downstream of the trailing edge, as predicted by the four-equation transitional shear stress transport (SST) and the LES WALE models, exhibit notable agreement. While LES typically resolves more turbulence details and provides better accuracy in simulating roughness effects, the comparison between LES and RANS resulted in similar wake profiles. This outcome provided the necessary confidence to proceed with LES simulations of surface roughness without conducting a full LES mesh independence study, particularly given the limitations in computational resources. Despite these constraints, the strong correlation between LES, RANS and experimental wind tunnel cascade data supports the robustness of the CFD simulations and validates the use of LES for further roughness analysis.



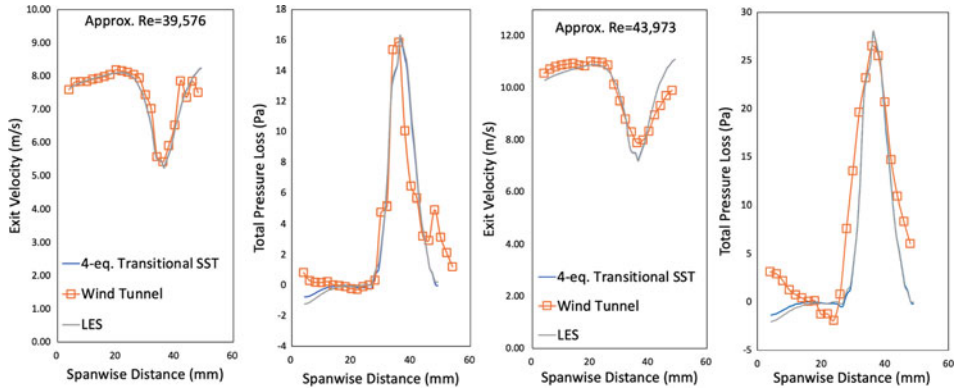


**Figure 13.** *Wren100 stator smooth mean profile exit velocity and total pressure loss (CFD Vs. wind tunnel cascade).*

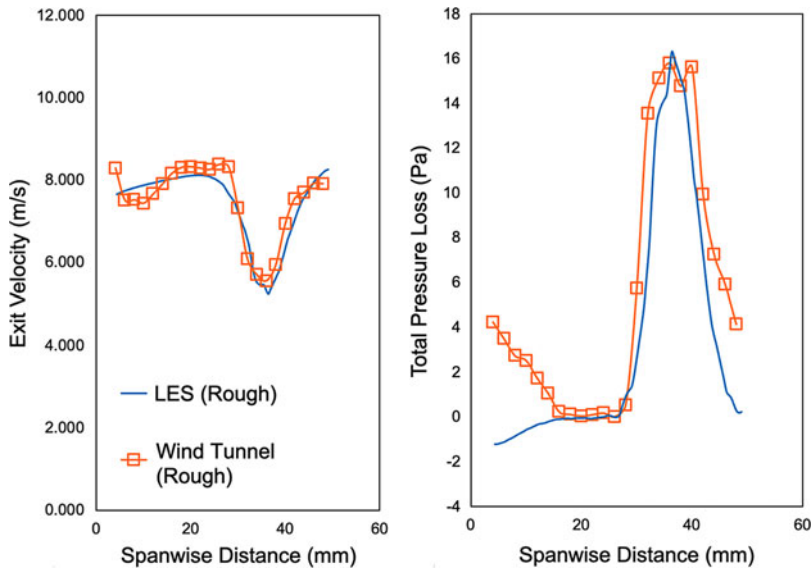


**Figure 14.** *Spanwise exit velocity and total pressure loss (LES vs. wind tunnel) ( $Re = 40,000$ ).*

## 7.2 Rough model (discrete)

The models used to investigate the impact of surface roughness assume the same sand grain roughness is uniformly distributed on the Wren100 stator vane cascade model. As mentioned earlier, instead of directly modifying the model surface, the ANSYS CFX utilises the input sand grain roughness and user-selected wall function to mimic the flow behaviour influenced by the rough surface.

Based on the wind tunnel data with the matched roughness Reynolds number, the simulation results of spanwise exit velocities and total pressures were validated against the experimental data as shown in Fig. 14.

From Fig. 14, it can be seen that the LES WALE model can capture the location and thickness of the trailing edge wake with good precision. Considering the limitations of the experimental measurements and the CFD model, the LES WALE model can predict the impact of surface roughness for the MGT with appropriate precision.

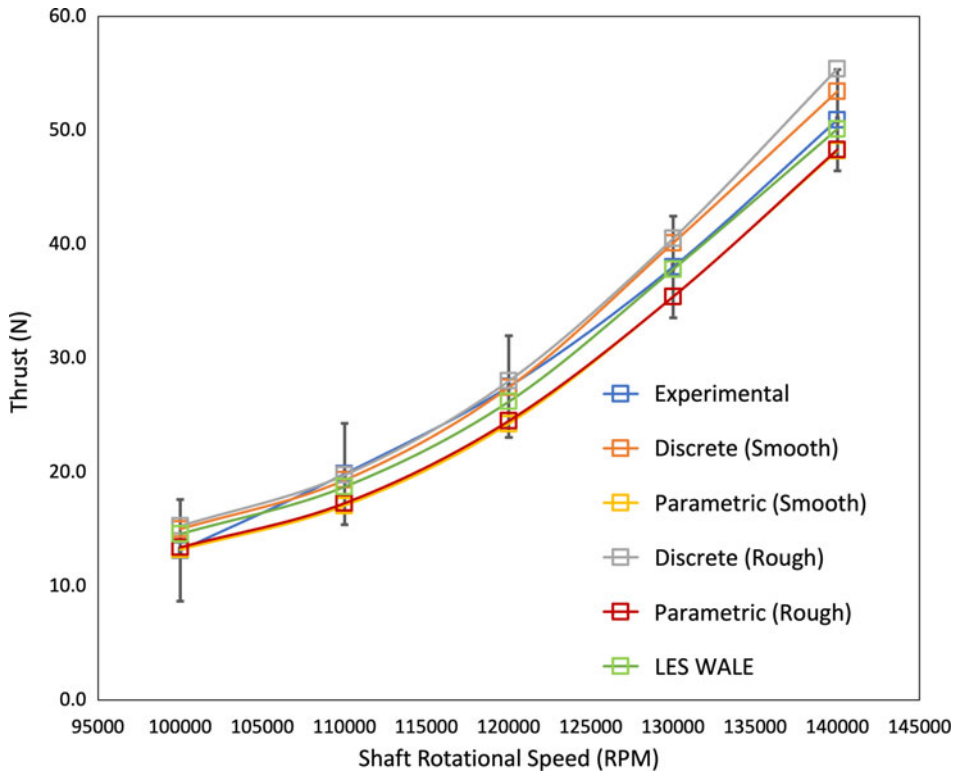


Figure 15. Wren100 turbine thrust at different RPMs (experimental vs. CFD).

## 8.0 Results and discussion

### 8.1 RE Model selections: pros and cons

To verify the accuracy of the RE models, a comparison was conducted between time-averaged experimental data and CFD predictions of the Wren100 engine thrust within a rotational speed range of 100,000–140,000RPM as shown in Fig. 15. The measurement uncertainties associated with the thrust sensor and rotational speeds were estimated to be  $\pm 4.45\text{N}$  and  $\pm 100\text{RPM}$ , respectively. High-fidelity large eddy simulations using the WALE turbulence model were performed and compared against both the transitional model and experimental data. This approach was adopted to evaluate the accuracy and predictive capabilities of the CFD models under consideration.

Based on the findings presented in Fig. 15, it was found both the discrete and parametric models could accurately represent the MGT performance at normal operating speeds from 100,000 to 140,000rpm, despite a limited set of blade parameters input requirements for the parametric model. According to these results, it is concluded that the engineer should focus on ‘what the part really is’ (discrete model) for the MGT performance analysis, such as the impact of surface roughness and ‘what the part should be’ (parametric model) for blade redesign. The reasons are listed in Table 6.

### 8.2 Wren100 MGT stator-rotor stage modelling with roughness

As shown in Table 7, it can be seen that there is a large influence of the Reynolds number and surface roughness on the loss of the MGT. In the case of the MGT stator operating at 120,000RPM exhibits marginal variations in the stagnation pressure loss coefficient ( $Y_p$ ). Previous analysis of the flow field properties ascertains that at the rotational speed of 120,000RPM, the boundary layer exhibits a substantial thickness. Consequently, the original surface roughness may not be sufficiently large to cause any

**Table 6.** Comparison of advantages and disadvantages of reverse engineering models

Model type	Advantages and disadvantages
Parametric model	Advantages: <ul style="list-style-type: none"> <li>- Requires limited blade parameters</li> <li>- Allows rapid adjustments to blade parameters</li> </ul> Disadvantages: <ul style="list-style-type: none"> <li>- Potential oversimplification of geometry</li> <li>- May miss critical aerodynamic features</li> </ul>
Discrete model	Advantages: <ul style="list-style-type: none"> <li>- Provides accurate representation of complex shapes</li> <li>- Effective for detailed aerodynamic analysis</li> </ul> Disadvantages: <ul style="list-style-type: none"> <li>- Higher computational cost</li> <li>- Longer processing time required</li> <li>- Involves extensive data handling</li> </ul>

**Table 7.** MGT discrete model performance with surface roughness based on LES WALE

Case	$T_{02}$ (k)	Thrust (N)	$\eta$ (%)	$Y_{p, \text{stator}}$ (%)	$Y_{p, \text{rotor}}$ (%)	RPM
Smooth	719.034	26.24	81.2	6.88	32.49	120k
Original SG	715.436	26.21	79.9	6.73	40.58	120k
30 $\mu\text{m}$ SG	717.272	26.45	80.0	8.41	37.78	120k
60 $\mu\text{m}$ SG	716.733	26.34	77.1	7.77	44.22	120k

significant perturbations in the boundary layer flow as it is within the laminar sublayer. However, an increase in roughness to 30 $\mu\text{m}$  sand grain (SG) and 60 $\mu\text{m}$  SG causes an upward trend in aerodynamic loss, which suggests that the boundary layer might be receptive to disturbances, increasing the losses.

For the rotor, the impacts of surface roughness on performance are greater compared to the stator. This can be attributed to the smaller chord sizes and so lower Reynolds number. No discernible trend can be seen as surface roughness progresses from a smooth surface to 60 $\mu\text{m}$  SG. However, a general increase in rotor roughness is accompanied by an escalation in aerodynamic losses.

### 8.3 Impact on the MGT stator trailing edge wakes

No previous studies have analysed how the roughness influences the TE wake for MGTs. For the Wren100 stator vanes, the phase-averaged relative velocities for different levels of SG roughness at the mean span were plotted across the span.

Figure 16 shows the complex relationship between the wake depth and the SG roughness. As the roughness increases, the size and depth of the TE wake increase as expected. However, as the SG roughness rises from 30 to 60 $\mu\text{m}$ , the wake size and depth reduce around 20.46%. It seems there exists an 'optimal' roughness size that induces the greatest turbulence and wake deepening, which in this specific MGT is around 30 $\mu\text{m}$  SG. However, when roughness exceeds this critical level of 60 $\mu\text{m}$  SG, it leads to a thicker, more separation-resistant boundary layer. This could limit the formation of secondary flows, thereby reducing the wake depth, which reduces the stagnation pressure loss from 8.41% to 7.77% as listed in Table 7. This unusual flow behaviour could be caused by the local flow features such as secondary flow and vortex shedding. At a certain level of SG roughness (30 $\mu\text{m}$ ), those flow structures would increase the wake depth. However, the same flow structures could inhibit the wake formations for other roughness levels. In addition, compared to the smooth and 30 $\mu\text{m}$  SG cases, the original SG and

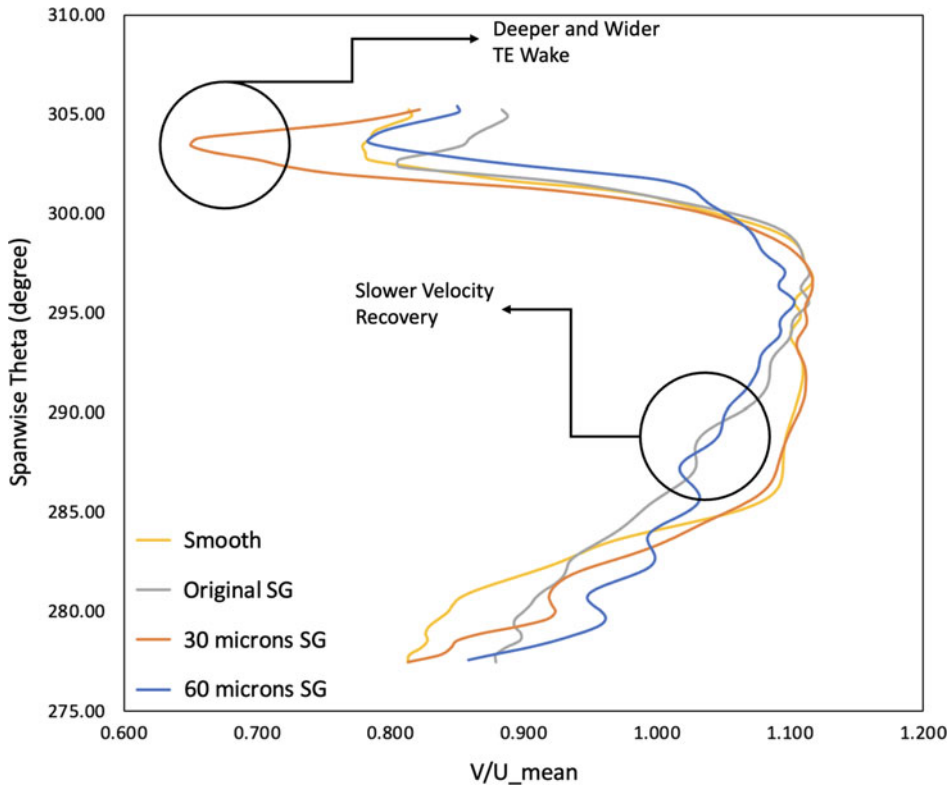


**Figure 16.** Phase-averaged spanwise relative velocities 10% chord after the Wren100 stator TE for different levels of roughness (120,000RPM).

60 $\mu$ m SG share similar velocity recovery behaviours outside the wake regions (slightly slower). This could be caused by several factors, including the enhanced strength of secondary flow structures due to the different boundary layer states or the altered transition location as the roughness level changes. Previous studies have also shown how rough-wall boundary layers cause big changes to secondary flow structures. Based on experimental studies, Vanderwel and Ganapathisubramani proved that secondary flows could be directly influenced by the spacing of surface roughness and developments of boundary layers [52]. Coull et al. numerically studied a turbine cascade, and they also discovered that larger secondary flow structures with higher SKE (secondary kinetic energy) could be caused by the thickening of the inlet boundary layer [53].

#### 8.4 Impact on the MGT stator vane boundary layer

As shown in Fig. 17, the phase-averaged skin friction coefficient magnitudes were plotted.

For relatively low Reynolds number turbine blades, it is known that increased surface roughness tends to reduce laminar separation bubbles (thus reducing loss). Compared to the pressure side, the suction side appears to be more sensitive to the roughness, which can be visualised by the sudden increase of skin friction as seen in locations SM1 and SM2. The local peak of skin friction on the suction side positioned about 15% chord downstream of the leading edge is caused by the flow separation behaviour near the leading edge.

It was found from the velocity vectors that the flow separation reduces rapidly as surface roughness increases, which the changes in boundary layer development can also be visualised in Figs 18 and 19.

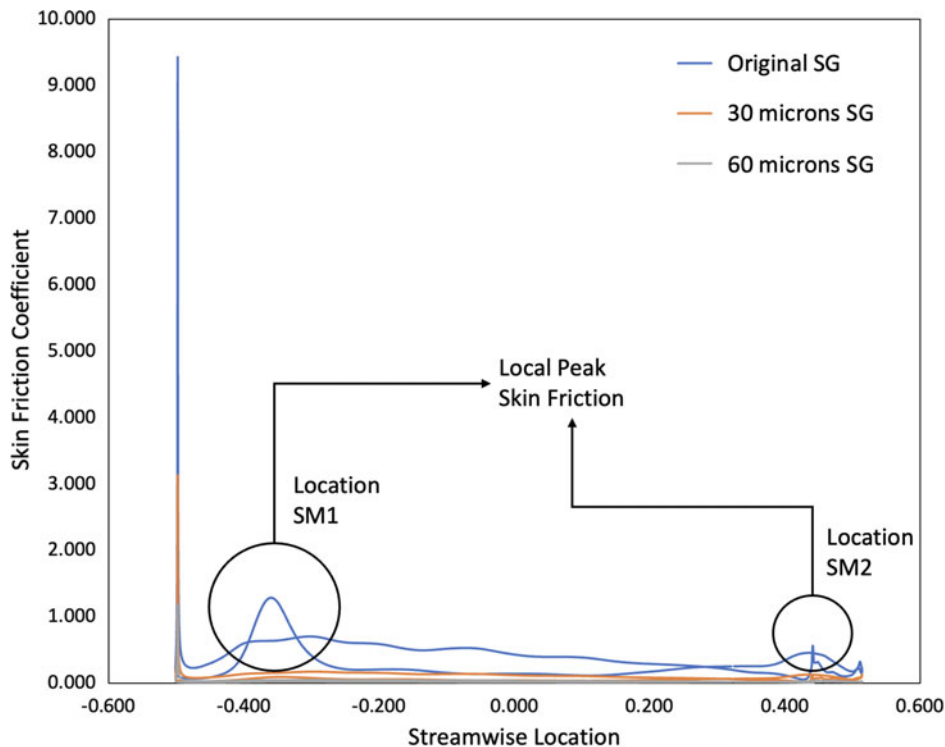


**Figure 17.** Phase-averaged Wren100 stator mean streamwise skin friction magnitude for different levels of roughness (120,000RPM).

The  $U_{98}$  plots were created on the mean span to further investigate the impact of roughness on the boundary layer development. At location 1, the thickening of the boundary layer ( $70.4\mu\text{m}$ ) is caused by flow separation. This transition from laminar to turbulent flow facilitates reattachment and prevents further separation in that region. Between surface roughness levels of  $30\mu\text{m}$  SG and  $60\mu\text{m}$  SG, a reduction of the local peak in skin friction after the leading edge is observed. Higher roughness typically reduces laminar separations in low Reynolds number flows, likely by promoting an earlier transition to turbulence. Consequently, it is possible that roughness at location 1 is delaying or suppressing flow separation and reducing the boundary layer thickness from  $70.4$  to  $2.2\mu\text{m}$ , as shown in Figs 18 and 19.

From Fig. 18, the original SG roughness ( $14.5\mu\text{m}$  SG) reduces the boundary layer thickness in all the monitored locations of the MGT stator vane. The regional rapid thinning of the boundary layer at location 1 is caused by the reduction of the leading edge flow laminar separation, thus lowering the overall stator pressure loss compared to the smooth case in Table 7. Hummel et al. found smaller profile loss for the roughened blade compared to the smooth ones at a slightly higher exit Reynolds number range (around 560,000). It was stated that the low Reynolds number benefit from surface roughness would only occur if the laminar separation on the smooth wall is prevented by roughness-induced transition [54]. For the stator at a Reynolds number of around 60,000, it can be seen that the increase in surface roughness eliminates the laminar separation bubble at location 1.

At locations 2 and 3, the velocity vectors revealed that the influence of surface roughness is less significant than at location 1. In the smooth case, the boundary layer at these locations is thinner due to the laminar separation bubbles near the leading edge. However, as roughness increases to  $60\mu\text{m}$  SG, the boundary layer thickens compared to the suction side near the leading edge. This suggests that the flow transitions from laminar to turbulent downstream of the stator vane, potentially due to roughness-induced flow instability.

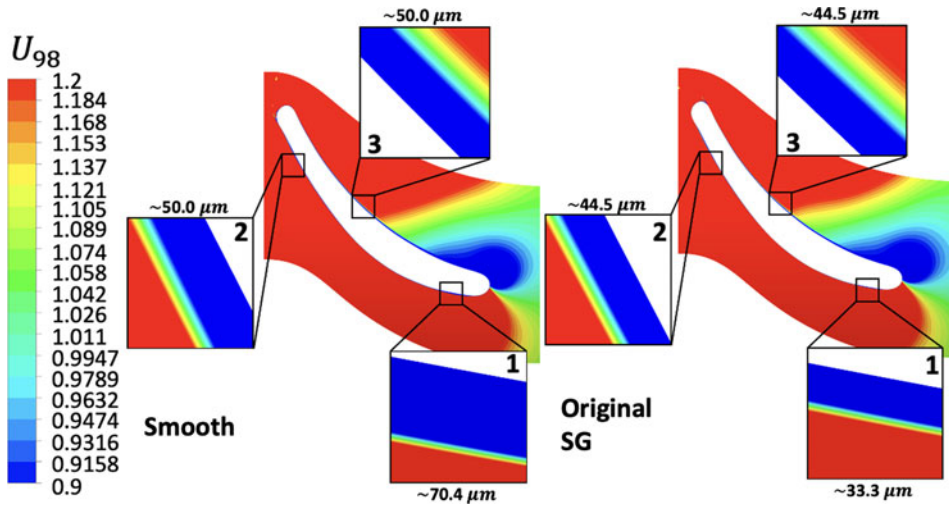


Figure 18. Wren100 MGT stator mean span boundary layer developments (left: smooth; right: original SG) (instantaneous plots, Phase 1.0).

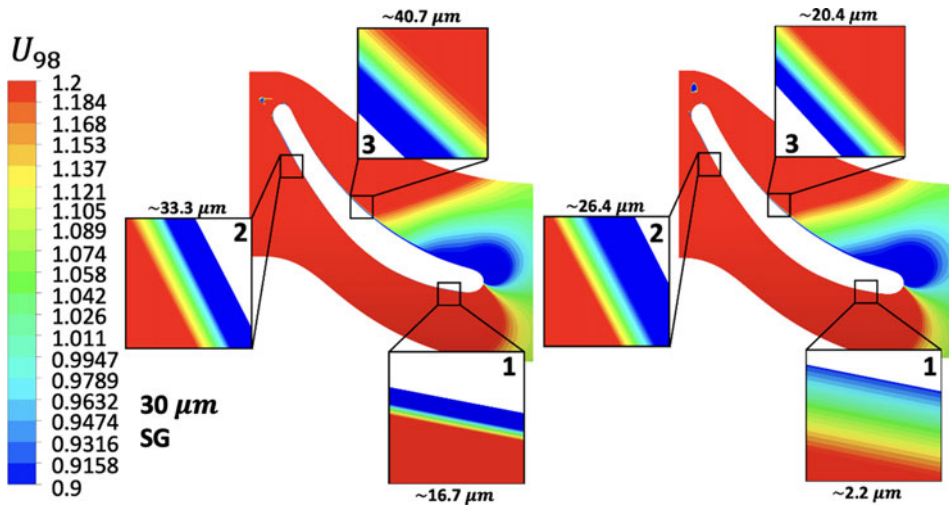


Figure 19. Wren100 MGT stator mean span boundary layer thickness (Left: 30μm SG; Right: 60μm SG) (Instantaneous Plots, Phase 1.0).

For the low Reynolds number flows here, the increase of surface roughness eliminates the laminar separation bubbles that originally occurred on the leading edge suction side in the smooth case. As the flow no longer separates, the flow remains laminar until it accelerates near the trailing edge. However, as roughness increases from the original SG to 60μm SG, the roughness increase seems to stabilise the flow and delay the flow transition. This explains the loss reduction and then increase around the original SG (14.5μm SG) as listed in Table 7. The sudden change in the boundary layer thinning rates for the 30μm SG case also indicates the existence of an ‘optimal’ roughness, which induces the greatest overall aerodynamic loss.



**Table 8.** Wren100 MGT rotor tip span instantaneous boundary layer thickness (instantaneous, Phase 1.0)

Smooth	Original ( $\sim 14.5\mu\text{m}$ ) SG	$30\mu\text{m}$ SG	$60\mu\text{m}$ SG
$227.3\mu\text{m}$	$83.3\mu\text{m}$	$134.3\mu\text{m}$	$17.1\mu\text{m}$

This table presents the boundary layer thickness on suction side of the rotor blade near its trailing edge.

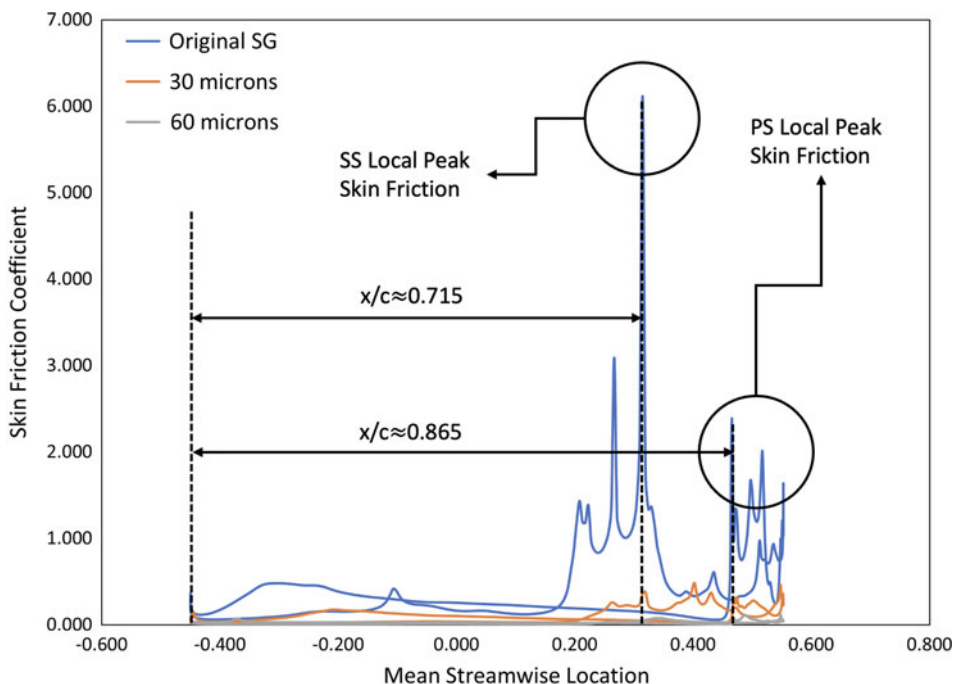


**Figure 20.** Phase-averaged Wren100 rotor mean streamwise skin friction magnitude for different levels of roughness (120,000RPM).

### 8.5 Impact on the MGT rotor blade boundary layer

As displayed in Fig. 20, the average skin friction coefficients across the rotor blade mean span drop rapidly as the surface roughness level increases from the original SG to  $60\mu\text{m}$  SG (at a Reynolds number of around 60,000). With the original SG roughness, multiple sudden increases in the skin friction coefficient magnitude on the suction side ( $x/c \approx 0.715$ ) are observed. These flow separation behaviours can also be shown in Table 8, where the cross-passage flow causes the thickening of the boundary layers on the suction side of the blade (SS). As the roughness level increases to  $30\mu\text{m}$  SG and  $60\mu\text{m}$  SG, the boundary layer near the trailing edge becomes less obvious, resulting in the reducing effects of the local peaks of skin friction.

Secondary flows can potentially increase as surface roughness changes from original SG to  $30\mu\text{m}$ . At  $30\mu\text{m}$  SG, the increased secondary flow effects and roughness-induced flow transition could very likely be the cause for the observed thickening of the boundary layer at the mean span at the examined location. However, as the roughness further increases to  $60\mu\text{m}$  SG, boundary layer thickness is rapidly reduced and more streamlined flow. From the velocity vector diagrams, almost no flow separation is visible. For the original roughness case, the skin friction surges are likely caused by the potential transition behaviour before the flow leaves the blade trailing edge. As the surface roughness further increases, the flow becomes more stabilised, resulting in a more flattened skin friction coefficient distribution.



**Table 9.** MGT rotor blade near tip separation onset locations for different levels of surface roughness

	Original SG (~ 14.5 $\mu$ m)	30 $\mu$ m SG	60 $\mu$ m SG
Separation onset/axial chord	26.4%	33%	51.7%

This table presents the separation onset distances as percentages of the axial chord length for different surface roughness conditions on the rotor blade tip.

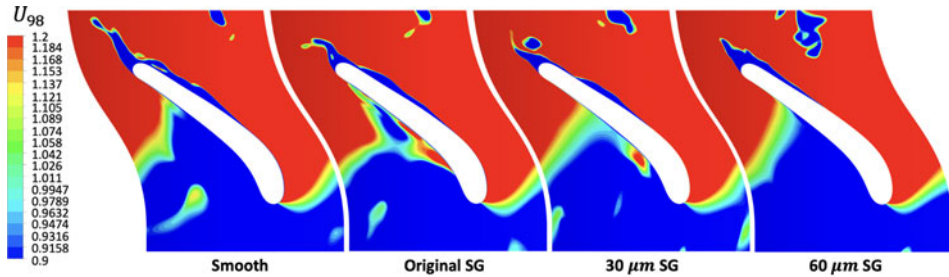


**Figure 21.** Wren100 MGT rotor tip span instantaneous boundary layer thickness (instantaneous plots, Phase 1.0).

For the near tip span, the flow behaviour becomes more complex due to the presence of the tip gap, which introduces additional secondary flows, such as tip leakage vortex and corner vortex, into the mainstream flow. As surface roughness increases, the overall skin friction decreases, and the boundary layer becomes thinner (Fig. 21). However, the observation of numerous local increases of skin friction in the rear half of the blade with less reduction in of these peaks with increased roughness from original SG to 30 $\mu$ m SG is intriguing. This can also be noticed from the  $U_{98}$  boundary layer plots, where the thinning effect from original SG to 30 $\mu$ m SG is slightly less obvious than the mean span.

From the velocity vectors diagrams in Fig. 22, the wake formed after the blade trailing edge becomes smaller as the roughness increases to 30 $\mu$ m SG. However, the wake grows bigger when the blade surface is roughened to 60 $\mu$ m SG. Table 7 and the velocity vectors show that the roughness elements can potentially alter the wake structure and the loss generation in MGT blades. A similar influence due to the increased roughness was discussed in the stator case. Additionally, it can be clearly seen that the maximum height and length of the separation bubble decrease as the roughness level increases from the original SG to 30 and 60 $\mu$ m SG. Interestingly, the roughened blade also delays the separation bubble onset location (as listed in Table 9). On the near-tip span, the interaction between the rough surface and the tip leakage flow can potentially modify the characteristics of the tip leakage vortex, influencing the onset and extent of separation bubbles.

To sum up, for the rotor blade operating at 120,000RPM, increased surface roughness appears to mitigate local peaks of skin friction associated with secondary flows and flow separations. Instantaneous snapshots, like those shown from Fig. 22, illustrate these effects, but it is important to note that they are representative of broader trends observed across multiple instances in time, providing a reliable basis for these conclusions. At the mean span, higher surface roughness reduces the height and length of the separation bubble, although the onset location of separation remains constant. However, the flow fields remain highly complex in the hub and tip regions due to endwall interactions. The interaction between the main passage boundary layer and high-shear-stress zones on the blade surface near the tip creates several local skin friction peaks. Near the blade tip, an increase in roughness results in a smaller separation bubble, with the onset of separation occurring later. For roughness levels below 30 $\mu$ m SG, the tip leakage and corner vortices remain stable despite the heightened turbulence caused by larger roughness elements, producing local skin friction peaks. Once roughness levels reach 60 $\mu$ m SG, however, the heightened turbulence in the main passage begins to dominate, diminishing the influence of secondary flow features.

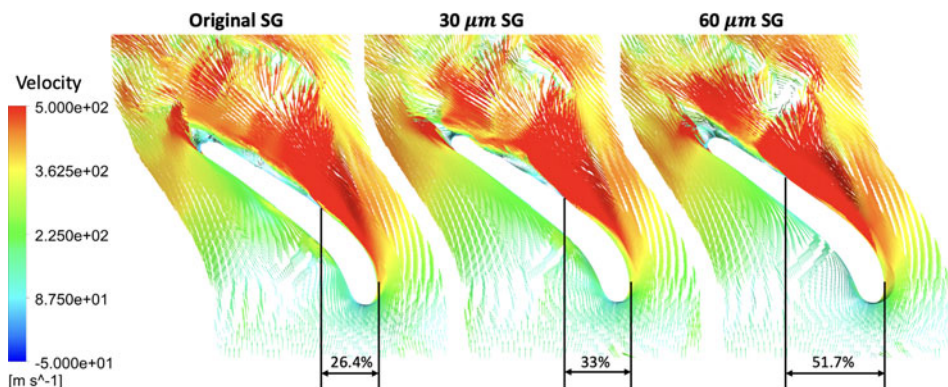


**Figure 22.** Instantaneous velocity vectors MGT rotor blade near tip span (instantaneous plots, Phase 1.0).

## 9.0 Conclusions

This paper demonstrates the effective use of silicone rubber moulds and EP resin tooling for accurately recreating complex, small-scale objects like MGT blades. Surface roughness measurements confirm that the discrepancy in roughness between the EP resin models and the actual turbine parts is minimal, at less than  $3\mu\text{m}$ .

Two reverse-engineering strategies were employed to construct 3D models of the stator and rotor. These models were then analysed using CFD simulations to evaluate their aerodynamic performance, using a transitional turbulence model to capture the flow at the low Reynolds numbers found here. Experimental tests across a range of Reynolds numbers from 40,000 to 90,000 provided the initial boundary conditions for the CFD simulations and served to validate the computational findings through wind tunnel validation.

Analysis revealed that the discrete model had marginally closer performance predictions than the parametric model. This superiority stems from the inclusion of all the blade characteristics within the discrete model, suggesting one must focus on ‘what the part really is’ geometry of parts compared to ‘what the part could be’ scenarios created by the parametric model.

The wind tunnel cascade experiments and LES WALE model simulations at Reynolds number of around 60,000 showed there was an ‘optimal’ surface roughness maintenance where the loss was at a maximum. It was observed that surface roughness could eliminate laminar separation bubbles near the leading edge on the suction side, potentially delaying the onset of flow transition. This roughness was shown to reduce the effects of secondary losses. For the rotor tip, increased surface roughness was found to reduce the size of the separation bubble and delay its onset.

Overall, this paper underscores the necessity of exploring the effects of varying low Reynolds numbers on aerodynamic losses on MGT.

**Acknowledgements.** The authors would like to thank Turbine Power Solutions Ltd. for supplying the Wren100 engine unit.

## References

- [1] Ren, L., Zhu, R., Liao, L. and Zhou, Y. Analysis on the development of micro gas turbine generation technology, *J. Phys. Conf. Ser.*, 2021, **1983**, (1), p 012006.
- [2] AMT Netherlands. AMT Netherlands Mercury HP, Amtjets.com, 2022, <http://www.amtjets.com/MercuryHP.php>
- [3] Bf-turbines. Turbine B100F, Bf-turbines.de, 2022, <http://www.bf-turbines.de/>
- [4] Jetcat Company. P100-RX - JetCat, Jetcat.de, 2022, [https://www.jetcat.de/en/productdetails/produkte/jetcat/produkte/hobby/Engines/p100\\_rx](https://www.jetcat.de/en/productdetails/produkte/jetcat/produkte/hobby/Engines/p100_rx)
- [5] Hawkturbine. Hawk 100R, Hawkturbine.com, 2022, <http://www.hawkturbine.com/Hawk100R1.htm>

- [6] Turbine Power Solutions Ltd. Wren Engine Sales and Service, Fuel Tubing, Pneumatic Fittings, RC Jets - Turbine Solutions, Turbinesolutions.co.uk, 2022, <https://www.turbinesolutions.co.uk/>
- [7] Kumar, R., Kumar, V., Butt, M., Sheikh, N., Khan, S. and Afzal, A. Thermo-mechanical analysis and estimation of turbine blade tip clearance of a small gas turbine engine under transient operating conditions, *Appl. Therm. Eng.*, 2020, **179**, p 115700.
- [8] Benini, E. *Progress in Gas Turbine Performance*, Scitus Academics Llc, 2016, pp 107–109.
- [9] Nascimento, M., De, L., Santos, E., et al. Micro Gas Turbine Engine: A Review, 2013.
- [10] ACARE, Protecting the environment and the energy supply | Acare, Acare4europe.org, <https://www.acare4europe.org/sria/flightpath-2050-goals>
- [11] Raja, V. and Fernandes, K. *Reverse Engineering*, Springer, 2010, London.
- [12] Gamil, A.A., Nikolaidis, T., Teixeira, J.A., Madani, S.H. and Izadi, A. Assessment of surface roughness effects on micro axial turbines, Turbo Expo: Power for Land, Sea, and Air, 2021, vol. 84195, p V008T20A031.
- [13] Bai, T., Liu, J., Zhang, W. and Zou, Z. Effect of surface roughness on the aerodynamic performance of Turbine Blade Cascade, *Propul. Power Res.*, 2014, **3**, (2), pp 82–89.
- [14] Várady, T., Martin, R. and Cox, J. Reverse engineering of geometric models—an introduction, *Computer-Aided Design*, 1997, **29**, (4), pp 255–268.
- [15] Langbein, F.C. Beautification of Reverse Engineered Geometric Models, PhD thesis, Dept. of Computer Science, Cardiff University, 2003.
- [16] Mahboubkhah, M., Aliakbari, M. and Burvill, C. An investigation on measurement accuracy of digitizing methods in turbine blade reverse engineering, *Proc. Inst. Mech. Eng. Part B J. Eng. Manuf.*, 2016, **232**, (9), pp 1653–1671.
- [17] Mohaghegh, K., Sadeghi, M. and Abdullah, A. Reverse engineering of turbine blades based on design intent, *Int. J. Adv. Manuf. Technol.*, 2006, **32**, (9-10), pp 1009–1020.
- [18] She, C. and Chang, C. Study of applying reverse engineering to turbine blade manufacture, *J. Mech. Sci. Technol.*, 2007, **21**, (10), pp 1580–1584.
- [19] Li, Y., Huang, X., Gong, C. and Wang, K. An engineering rules based parameterisation approach for turbine blade reverse engineering, *J. Math. Anal. Appl.*, 2004, **292**, (1), pp 311–315.
- [20] Zhang, L.N., Zhang, D.H. and Liu, Y.P. Research on modeling turbine blade in reverse engineering, *Mater. Sci. Forum*, 2006, **532-533**, pp 777–780.
- [21] Lakehal, D. Near-wall modeling of turbulent convective heat transport in film cooling of turbine blades with the aid of direct numerical simulation data, *Journal of Turbomachinery*, 2002, **124**, (3), pp 485–498. Available: <https://doi.org/10.1115/1.1482408>.
- [22] Guo, X., Wang, S., Li, X. and Ren, J. Aerothermodynamic features of a Coriolis-applied smooth U channel for gas turbine blade, *Int. J. Therm. Sci.*, 2024, **197**, p 108815.
- [23] Sofi, A.Y. and Qayoum, A. Heat transfer and fluid flow characteristics in a two pass duct with variable rib shapes: a CFD analysis, *Lect. Notes Mech. Eng.*, 2024, pp 457–469.
- [24] Karczewski, M. and Błaszczak, J. Performance of three turbulence models in 3D flow investigation for a 1.5-stage turbine, *Task Q.*, 2008, **12**, (3-4), pp 185–195.
- [25] Dong, P. and Amano, R.S. High-pressure gas turbine vane turbulent flows and heat transfer predicted by RANS/LES/DES, *Proceedings of the ASME Turbo Expo*, vol. 5B, 2017.
- [26] He, Y., Li, Y., Cai, L.-X., Yao, J.-W. and Hou, Y.F. Research on automatic aerodynamic performance optimization for flue gas turbine blades under multiple conditions, *Proceedings of the ASME Turbo Expo*, vol. 13D, v13dt34a009, 2023.
- [27] Kim, S., Suh, S., Baek, S. and Hwang, W. The effect of single-sided ribs on heat transfer and pressure drop within a trailing edge internal channel of a gas turbine blade, *J. Therm. Sci. Eng. Appl.*, 2022, **14**, (8), p 081005.
- [28] Xiao, K., He, J. and Feng, Z.-P. Study on the mechanism of cross flow suppression and heat transfer enhancement of alternating elliptical leading edge impingement chamber, *J. Eng. Thermophys.*, 2021, **42**, (11), pp 2816–2823.
- [29] Ju, Y., Feng, Y. and Zhang, C. Conjugate heat transfer simulation and entropy generation analysis of gas turbine blades, *J. Eng. Gas Turbines Power*, 2021, **143**, (8), p 081012.
- [30] Schreiner, B.D.J., Wilson, M., Li, Y.S. and Sanga, C.M. Effect of purge on the secondary flow-field of a gas turbine blade-row, *J. Turbomach.*, 2020, **142**, (10), p 101006.
- [31] Saleh, Z., Avital, E.J. and Korakianitis, T. Effect of in-service burnout on the transonic tip leakage flows over flat tip model, *Proc. Inst. Mech. Eng. Part A J. Power Energy*, 2020, **234**, (5), pp 655–669.
- [32] Jimenez, J. Turbulent flows over rough walls, *Ann. Rev. Fluid Mech.*, 2004, **36**, (1), pp 173–196.
- [33] Flack, K.A., Schultz, M.P. and Shapiro, K.D. Experimental support for Townsend's Reynolds number similarity hypothesis on rough walls, *Phys. Fluids*, 2005, (3).
- [34] ANSYS CFX-Solver Theory Guide, ANSYS Inc., 2023.
- [35] Flack, K.A. and Schultz, M.P. Roughness effects on wall-bounded turbulent flows, *Phys. Fluids*, 2014, **26**, p 101305.
- [36] Alldieck, R., Seehausen, H., Herbst, F. and Seume, J.R. The effect of rough-wall boundary conditions on RANS-based transition prediction, *Proceedings of Global Power, Propulsion Society*, 2020.
- [37] Blocken, B., Stathopoulos, T. and Carmeliet, J. CFD simulation of the atmospheric boundary layer: Wall function problems, *Atmos. Environ.*, 2007, **41**, (2), pp 238–252.
- [38] TECHNOVENT. Technical/User Data Sheet: Platinum Cure Rubber-Z004, *Technovent.com*, 2022, <http://www.technovent.com/Z004%20Instructions%20and%20MSDS.pdf>.
- [39] Bondmaster. Two Part Epoxy Resin Technical Information Sheet, *Farnell.com*, 2022, <http://www.farnell.com/datasheets/316730.pdf>

- [40] Alicona, B. InfiniteFocusSL, *Alicona.com*, 2022, <https://www.alicon.com/en/products/infinitefocuss/>
- [41] SHINING 3D, EinScan Pro 2X Plus-Handheld Industrial Scanner, *EinScan*, 2022, <https://www.einscan.com/handheld-3d-scanner/2x-plus/>
- [42] Amornvit, P. and Sanohkan, S. The accuracy of digital face scans obtained from 3D scanners: an in vitro study, *Int. J. Environ. Res. Public Health*, 2019, **16**, (24), p 5061.
- [43] Daemen, J.H.T., Loonen, T.G.J., Verhulst, A.C., Maal, T.J.J., Maessen, J.G., Vissers, Y.L.J., Hulsewé, K.W.E. and de Loos, E.R. Three-dimensional imaging of the chest wall: a comparison between three different imaging systems, *J. Surg. Res.*, 2020, **259**, pp 332–341.
- [44] manchestercfd. All there is to know about different mesh types in CFD!, *Grc.nasa.gov*, Manchester CFD.co.uk, 2020. [Online]. <https://www.manchestercfd.co.uk/post/all-there-is-to-know-about-different-mesh-types-in-cfd>
- [45] Simone, S., Montomoli, F., Martelli, F., Chana, K., Qureshi, I. and Povey, T. Analysis on the effect of a nonuniform inlet profile on heat transfer and fluid flow in turbine stages, *J. Turbomach.*, 2011, **134**, (1).
- [46] Sanders, D.D., O'Brien, W.F., Sondergaard, R., Polanka, M.D. and Rabe, D.C. Predicting separation and transitional flow in turbine blades at low Reynolds numbers—part I: development of prediction methodology, *J. Turbomach.*, 2011, **133**, (3), p 031011.
- [47] Kim, M., Lim, J., Kim, S., Jee, S. and Park, D. Assessment of the wall-adapting local eddy-viscosity model in transitional boundary layer, *Comput. Methods Appl. Mech. Eng.*, 2020, **371**, p 113287.
- [48] Odier, N., Duchaine, F., Gicouel, L., Dufour, G. and Park, D. Comparison of Les and Rans predictions with experimental results of the fan of a Turbofan, European Conference on Turbomachinery Fluid Dynamics and Hermodynamics, 2017.
- [49] Golchin, H., Ommi, F. and Saboohi, Z. Assessment of converting approach to efficient design of micro-turboprop engines, *Chin. J. Aeronaut.*, 2020, **33**, (2), pp 572–588.
- [50] Saravanamuttoo, H. *Gas Turbine Theory*, 7th ed, Licensing Agency Ltd., 2017, London.
- [51] Rory Douglas Stieger. The Effects of Wakes on Separating Boundary Layers in Low Pressure Turbines, PhD thesis, Cambridge University Engineering Department, Cambridge, UK, 2002. [Online]. [http://www-g.eng.cam.ac.uk/whittle/T106/T106A\\_cascade/T106A\\_cascade\\_publications/RStieger\\_PhD.pdf](http://www-g.eng.cam.ac.uk/whittle/T106/T106A_cascade/T106A_cascade_publications/RStieger_PhD.pdf)
- [52] Vanderwel, C. and Ganapathisubramani, B. Effects of spanwise spacing on large-scale secondary flows in rough-wall turbulent boundary layers, *J. Fluid Mech.*, 2015, **774**, pp. R2.
- [53] Coull, J., Clark, C. and Vazquez, R. The sensitivity of turbine cascade endwall loss to inlet boundary layer thickness, *J. Global Power Propul. Soc.*, 2019, **3**, pp. 540–554.
- [54] Hummel, F., Lötzerich, M., Cardamone, P., and Fottner, L. Surface roughness effects on turbine blade aerodynamics, *J. Turbomach.*, 2005, **127**, (3), p 453.